JOURNAL REVIEW

Thermal-Hydrodynamic Modeling of Bubbly Flows with Heat and Mass Transfer

G. H. Yeoh

Australian Nuclear Science and Technology Organisation (ANSTO), PMB 1, Menai, NSW 2234, Australia

J. Y. Tu

School of Aerospace, Mechanical and Manufacturing Engineering, RMIT University, Victoria 3083, Australia

A three-dimensional (3-D) two-fluid model coupled with the population balance equation is used to predict bubbly flows with the presence of heat and mass transfer processes, particularly on subcooled boiling flows at low pressures. To account for the nonuniform bubble distribution in the bulk liquid at subcooled conditions, the CFX MUSIG (MUltiple-Size Group) model is further developed by incorporating the wall nucleation at the heated wall and condensation in the flow regime. Model predictions, covering a wide range of different mass and heat fluxes and inlet subcooling temperatures, are compared against local and axial measurements. For the local case, the bubble size predictions include the comparison of the empirical bubble diameter relationships adopted in the CFX boiling model. The study shows that good agreement is better achieved by the present model with respect to the radial distributions of the bubble Sauter diameter, void fraction, interfacial area concentration, and liquid velocity profiles. However, significant weakness prevails over the vapor velocity distribution. Work is in progress to circumvent the deficiency by considering additional momentum equations or developing an algebraic slip model to account for bubble separation. For the axial case, good agreement is also achieved for the axial distributions of the mean bubble Sauter diameter, void fraction, and interfacial area concentration profiles. Here, the model correctly represents the plateau at the initial boiling stages at upstream, typically found in low-pressure subcooled boiling flows, followed by the significant increase of the void fraction at downstream. © 2004 American Institute of Chemical Engineers AIChE J, 51: 8–27, 2005

Introduction

Application of the population balance approach toward better describing and understanding complex industrial flow systems has received unprecedented attention. This has resulted in a number of significant developments, especially toward better designing bubble column reactors or other types of reactors that require large interfacial area for gas–liquid mass transfer and efficient mixing for competing gas–liquid reactions. Nevertheless, in many of these reactors, the rate of transport of the gas to the liquid often negates productivity. This aspect is a critical design criterion. To resolve this problem, there is still a great need to formulate a more fundamental understanding of the local hydrodynamics and rate processes. To achieve an optimum design, a more in-depth study, investigating the range of bubble sizes and thus the interfacial areas between the gas–liquid phase that may exist within the flow regime, is required.

With the advancement of computer technologies, the quest for improved designs has provided much impetus toward the use of numerical models. Recently, Ramkrisha and Mahoney[1]
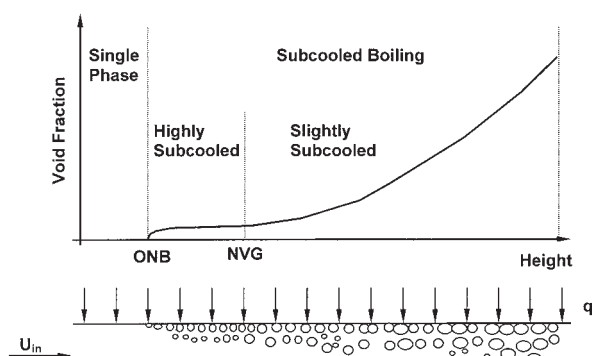
Figure 1. Subcooled flow boiling regions.

reviewed the applications of population balance models to a number of industrial problems. These models have been shown to possess tremendous potential and have a promising future toward handling complex two-phase flow systems. Several numerical studies, using the methodology of computational fluid dynamics (CFD), have been conducted.[2-5] The coupling between the CFD and population balance models has expedited a more thorough understanding of different flow regimes. They have also further enhanced a better understanding of the bubble mechanisms, especially with the consideration of bubble coalescence and breakup mechanisms in the model simulations.

Although considerable efforts have been invested to develop more sophisticated models for bubble migration, attention of the transport processes is still very much focused on isothermal bubbly flow problems. Wu et al.,[6] Hibiki and Ishii,[7,8] Hibiki et al.,[9] and Ishii et al.[10] all formulated an interfacial area transport equation for two-phase turbulent flows. This transport equation may be regarded as a simpler form of the population balance equation in determining the range of bubble sizes in the flow volume. In a finite-control volume, the currently applied population balance models, as reviewed by Ramkrisha and Mahoney,[1] track the distribution of various bubble sizes that may exist in the bulk liquid. The interfacial area transport approach, however, determines only average values of the bubble size based on the average distributions of the interfacial area and void fraction in the same control volume. This approach also aims to categorize various types of bubbles into groups, such as two-group interfacial area transport equations covering the range of bubbles from bubbly-to-slug flow transition, which are the spherical/distorted bubble group and the cap/slug bubble group. Along similar developments, Milles and Mewes[11] and Lehr and Mewes[12] formulated a transport equation for the interfacial area density (average bubble volume) to resolve the bubble mechanistic behaviors in bubble columns.

There is an increasing need to develop a more robust mathematical model capable of handling complex phenomena associated with hydrodynamics, heat and mass transfer, and bubbles undergoing coalescence and breakup. The subcooled boiling flow, which belongs to a specific category of bubbly flows, embraces all the complex dynamic interactions of the above-mentioned phenomena. Here, heterogeneous bubble nucleation occurs within small pits and cavities on the heater surface, designated as nucleation sites. These nucleation sites are activated when the temperature of the surface exceeds the saturation temperature of the liquid at the local pressure. If the temperature of the bulk fluid remains below saturation at the same location, the boiling process is known as *subcooled flow boiling*. Subcooled flow boiling is thus characterized by a *high-temperature* two-phase region near the heated wall and a *low-temperature* single-phase liquid away from the heated surface, as depicted in Figure 1. Subcooled boiling starts at a point called the *onset of nucleate boiling* (ONB). It continues downstream from the ONB point until the void fraction begins to increase sharply at a location called the *net vapor generation* (NVG). The NVG point is the transition between two regions: low void fraction region followed by a second region, in which the void fraction increases significantly.

In our investigation of axial void fraction distribution in channels, significant improvements made to the boiling flow model contributed to good agreement of the model predictions against a wide range of experimental data.[13,14] Nevertheless, further investigations in Yeoh et al.,[15] against local radial measurements of Lee et al.[16] for a low-pressure subcooled boiling annular channel flow, revealed a significant weakness of the model, primarily in the radial prediction of the bubble Sauter diameter and liquid and vapor velocities. The empirical correlation applied for our axial comparison exercise that determined the bubble size in the bulk subcooled liquid was derived to predict only the macroscopic consideration of the boiling phenomenon. It was thus not surprising that numerical models that use this sort of relationship were unable to adequately resolve the complex mechanistic behaviors of bubble coalescence and condensation (microscopic in nature) as observed through experiments. Experimental observations by Lee et al.,[16] using high-speed photography (see Figure 2), clearly depicted the presence of large bubble sizes away from the heated wall. The vapor bubbles, relatively small when detached from the heated surface, were seen to increase in size as a result of bubble coalescence. The bubbles, however, gradually decreased in size as a result of the increased condensation as they migrated toward the opposite end of the unheated wall of the annular channel. This phenomenon, commonly found in subcooled boiling flows, was further confirmed by experimental observations of Gopinath et al.[17] (see Figure 3), which illustrate a bubble gradually being condensed in a subcooled liquid away from the heated surface.

The absence of the bubble mechanistic behavior, such as bubble coalescence clearly observed during experiments in the vicinity of the heated wall and the condensation process being dominant in the unheated flow region, significantly compromised the model predictions (especially the bubble Sauter diameter distribution). In the two-fluid CFD model, which is the most commonly used macroscopic formulation of the thermal-hydrodynamics of the two-phase systems, the phasic interaction term appears in the field equations. These terms represent the important contribution of the
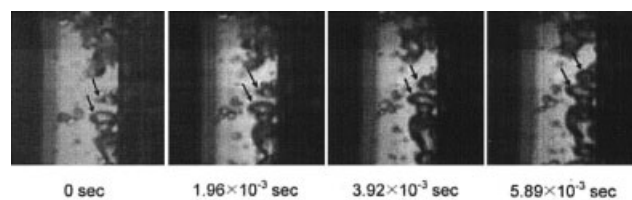

Figure 2. Significant bubble coalescence observed in the vicinity of the heated wall of an annular channel.[16]
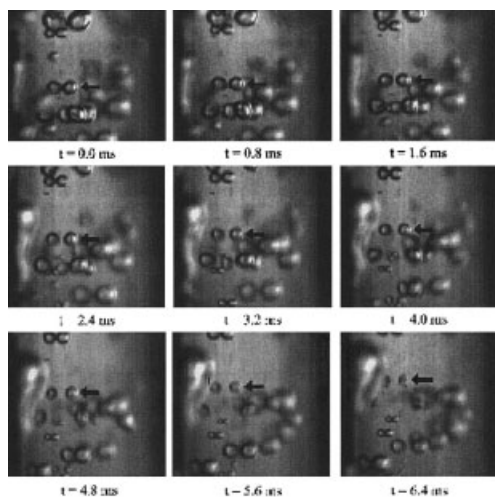
Figure 3. A bubble undergoing condensation in a sub-cooled liquid.[17]

mass, momentum, and energy transfers through the interface between the phases. An accurate determination of the bubble Sauter diameter is crucial because the bubble size influences the interphase heat and mass transfer through the interfacial area concentrations and momentum drag terms. Because of the successes in using the population balance approach, the potential to implement and extend the modeling to predict the nonuniform bubble size distribution in subcooled boiling flows is of enormous significance. Such a capability does not exist in the current state of the art. Therefore, a successful and specific development of the population balance approach for boiling flows can contribute to a significant improvement in formulation of the two-fluid boiling model.

The objectives of this present study are twofold: (1) to develop and formulate a population balance approach using the MUSIG (multiple-size group) model (developed originally by Lo[18]) coupled with a complete 3-D flow numerical simulation for subcooled boiling flows at low pressures, especially the inclusion of the important phenomenology of nucleation and condensation processes in the generic computer code CFX; and (2) to evaluate the new MUSIG boiling model through validation against experimental measurements. Comparisons of model predictions for a range of different mass and heat fluxes and inlet subcoolings are performed against axial measurements of Zeitoun and Shoukri[19] and local measurements of Yun et al.[20] and Lee et al.[16] The latter experiments allow comparisons of local radial quantities within the boiling channel, whereas the former experiments permit comparisons along the axial length of the test channel. The former will also help to assess the capability of the developed MUSIG boiling model in predicting the subcooled boiling flow characteristics depicted in Figure 1.

Mathematical Formulation

Flow equations

The two-fluid model, treating both the vapor and liquid phases as continua, solves two sets of conservation equations governing mass, momentum, and energy, which are written for each phase as:

Continuity Equation of Liquid Phase

$$\frac{\partial \rho_l \alpha_l}{\partial t} + \nabla \cdot (\rho_l \alpha_l \vec{u}_l) = \Gamma_{lg} \tag{1}$$

Continuity Equation of Vapor Phase

$$\frac{\partial \rho_g \alpha_g f_i}{\partial t} + \nabla \cdot (\rho_g \alpha_g \vec{u}_g f_i) = S_i - f_i \Gamma_{lg} \tag{2}$$

Momentum Equation of Liquid Phase

$$\frac{\partial \rho_l \alpha_l \vec{u}_l}{\partial t} + \nabla \cdot (\rho_l \alpha_l \vec{u}_l \vec{u}_l) = -\alpha_l \nabla P + \alpha_l \rho_l \vec{g}$$
$$+ \nabla \cdot \{\alpha_l \mu_l^e [\nabla \vec{u}_l + (\nabla \vec{u}_l)^T]\} + (\Gamma_{lg} \vec{u}_g - \Gamma_{gl} \vec{u}_l) + F_{lg} \tag{3}$$

Momentum Equation of Vapor Phase

$$\frac{\partial \rho_g \alpha_g \vec{u}_g}{\partial t} + \nabla \cdot (\rho_g \alpha_g \vec{u}_g \vec{u}_g) = -\alpha_g \nabla P + \alpha_g \rho_g \vec{g}$$
$$+ \nabla \cdot \{\alpha_g \mu_g^e [\nabla \vec{u}_g + (\nabla \vec{u}_g)^T]\} + (\Gamma_{gl} \vec{u}_l - \Gamma_{lg} \vec{u}_g) + F_{gl} \tag{4}$$

Energy Equation of Liquid Phase

$$\frac{\partial \rho_l \alpha_l H_l}{\partial t} + \nabla \cdot (\rho_l \alpha_l \vec{u}_l H_l) = \nabla \cdot [\alpha_l \lambda_l^e \nabla T_l]$$
$$+ (\Gamma_{lg} H_g - \Gamma_{gl} H_l) \tag{5}$$

Energy Equation of Vapor Phase

$$\frac{\partial \rho_g \alpha_g H_g}{\partial t} + \nabla \cdot (\rho_g \alpha_g \vec{u}_g H_g) = \nabla \cdot [\alpha_g \lambda_g^e \nabla T_g]$$
$$+ (\Gamma_{gl} H_l - \Gamma_{lg} H_g) \tag{6}$$

In Eq. 1, Γ_{lg} represents the mass transfer rate attributed to condensation in the bulk subcooled liquid, which is expressed by

$$\Gamma_{lg} = \frac{h a_{if}(T_{sat} - T_l)}{h_{fg}} \tag{7}$$

where h is the interphase heat transfer coefficient (determined from Ranz and Marshall[21]) Nusselt number correlation and a_{if} is the interfacial area between phases per unit volume. The wall vapor generation rate is modeled in a mechanistic way, derived by considering the total mass of bubbles detaching from the heated surface as

$$\Gamma_{gl} = \frac{Q_e}{h_{fg} + C_{pl} T_{sub}} \tag{8}$$

where Q_e is the heat transfer resulting from evaporation. This wall nucleation rate is accounted in Eq. 2 as a specified boundary condition apportioned to the discrete bubble class based on

the size of the bubble departure criteria on the heated surface. On the right-hand side of Eq. 2, S_i represents the additional source terms attributed to coalescence and breakup based on the formulations that are described in the next section. The term $f_i\Gamma_{lg}$ represents the mass transfer resulting from condensation redistributed for each of the discrete bubble classes. The gas void fraction along with the scalar fraction f_i are related to the number density of the discrete bubble ith class n_i (similarly to the jth class n_j) as $\alpha_g f_i = n_i v_i$. The size distribution of the dispersed phase is therefore defined by the scalar f_i. The population balance equation for each of the discrete bubble classes n_i is provided in the next section. Interphase transfer terms in the momentum and energy equations—Γ_{lg} and F_{lg}—denote the transfer terms from the gas phase to the liquid phase. The mass transfer Γ_{lg} is already given in Eq. 7, whereas the total interfacial force F_{lg} considered in the present study includes the effects of

$$F_{lg} = F_{lg}^{drag} + F_{lg}^{lift} + F_{lg}^{lubrication} + F_{lg}^{dispersion} \qquad (9)$$

The terms on the righthand side of Eq. 9 are the drag force, lift force, wall lubrication force, and turbulent dispersion force, respectively. Detailed descriptions of these forces can be found in Anglart and Nylund[22] and Lahey and Drew.[23] Briefly, the interphase momentum transfer between gas and liquid resulting from drag force is given by

$$F_{lg}^{drag} = \frac{1}{8} C_D a_{if} \rho_l |\vec{u}_g - \vec{u}_l|(\vec{u}_g - \vec{u}_l) \quad \text{and}$$

$$F_{lg}^{drag} = -F_{gl}^{drag} \qquad (10)$$

Lift force in terms of the slip velocity and the curl of the liquid phase velocity is described by

$$F_{lg}^{lift} = \alpha_g \rho_l C_L (\vec{u}_g - \vec{u}_l) \times (\nabla \times \vec{u}_l) \quad \text{and} \quad F_{lg}^{lift} = -F_{gl}^{lift} \qquad (11)$$

Wall lubrication force, which is in the normal direction away from the heated wall and decays with distance from the wall, is expressed by

$$F_{lg}^{lubrication} = -\frac{\alpha_g \rho_l (\vec{u}_g - \vec{u}_l)}{D_s} \max\left(0, C_{wl} + C_{w2}\frac{D_s}{y_w}\right)\vec{n}$$

$$\text{and} \qquad F_{gl}^{lubrication} = -F_{lg}^{lubrication} \qquad (12)$$

Turbulence-induced dispersion taken as a function of turbulent kinetic energy and gradient of the void fraction of the of liquid yields in the following form

$$F_{lg}^{dispersion} = -C_{TD}\rho_l \kappa \nabla \alpha_l \quad \text{and} \quad F_{gl}^{dispersion} = -F_{lg}^{dispersion} \qquad (13)$$

The drag coefficient C_D in Eq. 10 has been correlated for several distinct Reynolds number regions for individual bubbles according to Ishii and Zuber.[24] The constant C_L takes a value of 0.01, as suggested by Wang et al.[25] The wall lubrication constants C_{w1} and C_{w2}, as suggested by Antal et al.,[26] are −0.01 and 0.05, respectively. According to Kurul and

Podowski[27] the recommended value for C_{TD} of 0.1 is used for the turbulent dispersion force.

A two-equation κ–ε turbulence model is used for the continuous liquid and dispersed vapor phases. The effective viscosity in the momentum and energy equations is taken as the sum of the molecular viscosity and turbulent viscosity. The turbulent viscosity is considered as the total of the shear-induced turbulent viscosity and Sato's bubble-induced turbulent viscosity.[28]

The local bubble Sauter diameter, based on the calculated values of the scalar fraction f_i and discrete bubble sizes d_i, can be deduced from

$$D_s = \frac{1}{\sum_i \dfrac{f_i}{d_i}} \qquad (14)$$

Bubble nucleation, condensation, breakup, and coalescence model

According to Fleischer et al.,[29] the bubble size distribution is calculated with the following population balance equation

$$\frac{\partial n(V, \vec{x}, t)}{\partial t} + \nabla \cdot [\vec{u}_g n(V, \vec{x}, t)] = G(V, \vec{x}, t) \qquad (15)$$

where $n(V, \vec{x}, t)$ is the bubble number density distribution per unit mixture and bubble volume, which is a function for the spatial range $\vec{x}$ for a given time t and volume V. On the right-hand side, the term $G(V, \vec{x}, t)$ contains the bubble source/sink rates per unit mixture volume attributed to the bubble interactions such as coalescence, breakup, and phase change. For the case of nucleate boiling and condensation in a subcooled boiling flow, the phase-change term includes the rate of change of bubble population with specific volumes. Phenomenological models developed by Prince and Blanch[30] and by Luo and Svendsen[31] provided a detailed description of the mechanisms for coalescence and breakup of intermittent bubbles. To effectively use the number density transport equation given in Eq. 15, coupled with the above-mentioned phenomenological models of coalescence and breakup, Pohorecki et al.[4] suggested dividing Eq. 15 into N classes to classify the range of bubble sizes that may be present within the flow volume, that is

$$\frac{\partial n_i}{\partial t} + \nabla \cdot (\vec{u}_g n_i) = \left(\sum_j R_j\right)_i + (R_{ph})_i \qquad (16)$$

where $(\sum_j R_j)_i$ represents the net change in the number density distribution resulting from coalescence and breakup processes. This interaction term $(\sum_j R_j)_i (=P_C + P_B - D_C - D_B)$ contains the source rates of P_C, P_B, D_C, and D_B, which are, respectively, the production rates attributed to coalescence and breakup and the death rate to coalescence and breakup of bubbles formulated as

$$P_C = \frac{1}{2} \sum_{k=1}^{N} \sum_{l=1}^{N} \chi_{i,kl} n_i n_j$$

$$\chi_{i,kl} = \chi_{kl} \quad \text{if} \quad v_k + v_l = v_i \quad \text{else} \quad \chi_{i,kl} = 0 \quad \text{if} \quad v_k + v_l \neq v_i$$

$$P_B = \sum_{j=i+1}^{N} \Omega(v_j : v_i) n_j \qquad D_C = \sum_{j=1}^{N} \chi_{ij} n_i n_j \qquad D_B = \Omega_i n_i$$

$$(17)$$

The term $(R_{ph})_i$ in Eq. 16 constitutes the essential formulation of the source/sink rates for the phase change processes associated with subcooled boiling flow. At the heated surface, bubbles form at activated cavities known as active nucleation sites. The bubble nucleation rate from these sites can be expressed as

$$\phi_{WN} = \frac{N'' f \xi_H}{A_C} \tag{18}$$

where N'', f, ξ_H, and A_C are the active nucleation site density, the bubble generation frequency from the active sites, the heated perimeter, and the cross-sectional area of the boiling channel, respectively. Because the bubble nucleation process occurs only at the heated surface, this heated wall nucleation rate is not included in $(R_{ph})_i$ but rather specified as a boundary condition to Eq. 16, apportioned to the discrete bubble class n_i, based on the bubble departure criteria on the heated surface. The bubble sink rate resulting from condensation in a control volume for each bubble class can be determined from

$$\phi_{COND} = -\frac{n_i}{V_B} A_B \frac{dR_B}{dt} \tag{19}$$

The following holds for the bubble condensation velocity[17]

$$\frac{dR_B}{dt} = \frac{h(T_{sat} - T_l)}{\rho_g h_{fg}} \tag{20}$$

Substituting Eq. 20 into Eq. 19, and given that the bubble surface area A_B and volume V_B based on the bubble Sauter diameter are πD_s^2 and $\pi D_s^3/6$, respectively, Eq. 19 can be rearranged as

$$(R_{ph})_i = \phi_{COND} = -\frac{1}{\rho_g \alpha_g} \left(\frac{6\alpha_g}{D_s} \right) \left[\frac{h(T_{sat} - T_l)}{h_{fg}} \right] n_i$$

$$= -\frac{1}{\rho_g \alpha_g} \left[\frac{h a_{if}(T_{sat} - T_l)}{h_{fg}} \right] n_i \quad (21)$$

The breakup of bubbles in turbulent dispersions uses the model developed by Luo and Svendsen.[31] Binary breakup of the bubbles is assumed and the model is based on the theories of isotropic turbulence. The breakup rate of bubbles of volume v_j into volume sizes of v_i can be obtained as

$$\frac{\Omega(v_j : v_i)}{(1 - \alpha_g) n_j} = C \left(\frac{\varepsilon}{d_j^2} \right)^{1/3} \int_{\xi_{min}}^{1} \frac{(1 + \xi)^2}{\xi^{11/3}} \exp\left(-\frac{12 c_f \sigma}{\beta \rho_l \varepsilon^{2/3} d_j^{5/3} \xi^{11/3}} \right) d\xi$$

$$(22)$$

where $\xi = \lambda/d_j$ is the size ratio between an eddy and a particle in the inertial subrange and, consequently, $\xi_{min} = \lambda_{min}/d_j$; and C and β are determined, respectively, from fundamental consideration of drops or breakage of bubbles in turbulent dispersion systems to be 0.923 and 2.0. The variable c_f denotes the increase coefficient of surface area: $c_f = [f_{BV}^{2/3} + (1 - f_{BV})^{2/3} - 1]$, where f_{BV} is the breakage volume fraction.

The coalescence of two bubbles is assumed to occur in three steps. The first step involves the bubbles colliding, thereby trapping a small amount of liquid between them. This liquid film then drains until it reaches a critical thickness; and the last step features the rupturing of the liquid film, subsequently causing the bubbles to coalesce. The collisions between bubbles may be caused by turbulence, buoyancy, and laminar shear. Only the first cause of collision (turbulence) is considered in the present model. Indeed collisions caused by buoyancy cannot be taken into account here because all the bubbles from each class have been assumed to travel at the same speed. Moreover, calculations showed that laminar shear collisions are negligible because of the low superficial gas velocities considered in this investigation. The coalescence rate, considering turbulent collision taken from Prince and Blanch,[30] can be expressed as

$$\chi_{ij} = \frac{\pi}{4} [d_i + d_j]^2 (u_{ti}^2 + u_{tj}^2)^{0.5} \exp\left(-\frac{t_{ij}}{\tau_{ij}} \right) \tag{23}$$

where τ_{ij} is the contact time for two bubbles given by $(d_{ij}/2)^{2/3}/\varepsilon^{1/3}$ and t_{ij} is the time required for two bubbles to coalesce having diameter d_i and d_j estimated to be $\{(d_{ij}/2)^3 \rho_l / 16\sigma\}^{0.5} \ln(h_0/h_f)$. The equivalent diameter d_{ij} is calculated as suggested by Chesters and Hoffman[32]: $d_{ij} = (2/d_i + 2/d_j)^{-1}$. According to Prince and Blanch,[30] for air–water systems, experiments have determined the initial film thickness (h_0) and the critical film thickness at which rupture occurs (h_f) to be 1×10^{-4} and 1×10^{-8} m, respectively. The turbulent velocity u_t, in the inertial subrange of isotropic turbulence by Rotta,[33] is given by

$$u_t = 1.4 \varepsilon^{1/3} d^{1/3} \tag{24}$$

To account for the nonuniform bubble size distribution, bubbles ranging from 0 to 9.5 mm diameter for the local investigation and from 0 to 6.35 mm diameter for the axial investigation are equally divided into 15 classes (see Tables 1 and 2). These maximum bubble diameters of 9.5 mm for the local case and 6.35 mm for the axial case correspond to the channel gap sizes of the test sections. Instead of considering 16 different complete phases, it is assumed that each bubble class travels at the same mean algebraic velocity, to reduce the computational time, thus resulting in 15 continuity equations for the gas phase coupled with a single continuity equation for the liquid phase.

Table 1. Diameter of Each Discrete Bubble Class for the Local Case

Class No.	Central Class Diameter d_i (mm)
1	0.503
2	1.040
3	1.644
4	2.265
5	2.889
6	3.512
7	4.141
8	4.771
9	5.402
10	6.033
11	6.665
12	7.297
13	7.929
14	8.562
15	9.194

Wall heat partition model

Various experimental and theoretical investigations for low-pressure subcooled boiling flow by Judd and Hwang[34] suggest that the wall heat flux Q_w can be divided into three components: (1) heat transferred by conduction to the superheated layer next to the wall (nucleate boiling or surface quenching), Q_q; (2) heat transferred by evaporation or vapor generation, Q_e; and (3) heat transferred by turbulent convection, Q_c.

The surface quenching heat flux is determined through the following relationship

$$Q_q = \left[\frac{2}{\sqrt{\pi}} \sqrt{k_l \rho_l C_{pl}} \sqrt{f} \right] A_q (T_w - T_l) \tag{25}$$

where T_w is the wall temperature; A_q, the fraction of wall area subjected to cooling by quenching, is calculated from $A_q = N''(\pi d_{bw}^2/4)$; and f is the bubble generation frequency given by Cole[35]

$$f = \sqrt{\frac{4g(\rho_l - \rho_g)}{3 d_{bw} \rho_l}} \tag{26}$$

The bubble departure diameter d_{bw} is formulated from considering the balance of surface tension and buoyancy forces at low pressures[36]

$$d_{bw} = 2.496 \times 10^{-5} \left(\frac{\rho_l - \rho_g}{\rho_g} \right)^{0.9} \theta \left(\frac{\sigma}{g \Delta \rho} \right)^{0.5} \tag{27}$$

The density of active nucleation sites N'' is obtained from the data correlation of Lemmert and Chwalas,[37] which is expressed by

$$N'' = [210(T_w - T_{sat})]^{1.805} \tag{28}$$

The above relationship compares very well with subcooled boiling experimental data of Basu et al.[38] Based on the experimental observations of Zeitoun and Shoukri[19] and Lee et al.,[16] the bubble contact angles in Eq. 27 have been taken to be at 45 and 55° for the present investigation. These values are in accordance with the suggested range ($40° \leq \theta \leq 60°$) established in Hsu and Graham[39] for most industrial metals and water.

The heat flux attributed to vapor generation at the wall in the nucleate boiling region can be simply calculated from Bowring[40]

$$Q_e = N''f \left(\frac{\pi}{6} d_{bw}^3 \right) \rho_g h_{fg} \tag{29}$$

The heat flux according to the definition of local Stanton number St for turbulent convection is

$$Q_c = St \rho_l C_{pl} u_l (T_w - T_l)(1 - A_q) \tag{30}$$

It is noted that u_l is the local tangential liquid velocity adjacent to the heated surface.

Experimental Details

Experimental data of local subcooled boiling flow measurements performed by our Korean collaborators that are used for the current validation exercise were obtained from Yun et al.[20] and Lee at al.[16] The experimental setup consists of a vertical concentric annulus with an inner heating rod of 19 mm outer diameter. The heated section is a 1.67 m long Inconel 625 tube with 1.5 mm wall thickness and is filled with magnesium oxide powder insulation. The rod is uniformly heated by a 54-kW DC power supply. The outer wall consists of two stainless steel tubes with 37.5 mm inner diameter, which are connected by a transparent glass tube so that visual observation and photographic recording are made possible. The transparent glass tube is 50 mm long and is installed just below the measuring plane. The measuring plane is located at 1.61 m downstream of the beginning of the heated section. Demineralized water was used as the working fluid. The test channel inlet temperature was measured using the calibrated platinum resistance temperature detector with the estimated error of $\pm0.2°C$. The absolute pressure at the measuring plane was measured within the uncertainty of ±1 kPa. In this work, local gas-phase parameters, such as local void fraction, bubble frequency, and bubble velocity, were measured by a two-conductivity probe method, whereas the Pitot tube was used to measure the local measurement of liquid velocity with a mean relative error of 3.0%.

Table 2. Diameter of Each Discrete Bubble Class for the Axial Case

Class No.	Central Class Diameter d_i (mm)
1	0.336
2	0.699
3	1.099
4	1.511
5	1.928
6	2.347
7	2.768
8	3.189
9	3.611
10	4.033
11	4.455
12	4.878
13	5.300
14	5.723
15	6.146

Table 3. Experimental Conditions for Local Measurements: L1, L2, and L3

Run	P_{inlet} (MPa)	T_{inlet} (°C)	T_{sub}(inlet) (°C)	Q_w (kW/m²)	G (kg m⁻² s⁻¹)
L1	0.142	96.6	13.4	152.3	474.0
L2	0.137	94.9	13.8	197.2	714.4
L3	0.143	92.1	17.9	251.5	1059.2

However, the uncertainty of the bubble Sauter diameters (assuming spherical bubbles) determined through the interfacial area concentration (IAC), calculated using the measured bubble velocity spectrum and bubble frequency, was difficult to ascertain and will, at present, be estimated to be <27%. More details regarding the experimental setup can be found in Lee et al.[16] Experimental conditions used for comparison with the simulated results are presented in Table 3. Figure 4a shows a schematic drawing of the test channel.

For the axial measurements performed by Zeitoun and Shoukri,[19] the test section was a vertical concentric annular test section. The inner tube, which had a 12.7 mm outside diameter, was a 30.6 cm long, thick-walled stainless-steel tube (0.25 mm thick) that was electrically heated. The entire inner tube was connected to a 55-kW DC power supply. Accordingly, heat was generated uniformly along the axial length of the inner tube. The outer tube was a 25.4 mm inner diameter Plexiglas tube that permitted visual observation. Distilled–degassed water was used as the working fluid. A high-speed video system was used to collect the visual information to study bubble behavior upstream, near, and downstream of the NVG point. The uncertainty in determining the NVG location was ±2 cm. A digital image processing technique was used to analyze the high-speed video information and to measure bubble size distributions along the subcooled boiling region. Measured distances in the field of view were estimated to be accurate within ±0.05 mm. A single-beam gamma densitometer was used for void fraction measurements. Static calibration showed that the void fraction measurements were accurate within ±4%. Other measurements included the flow rate with an estimated error of ±2%. The test section inlet and outlet temperatures were calibrated using platinum resistance temperature detectors, as well as the liquid subcooling along the test section using J-type calibrated thermocouples. The uncertainties in the temperature and pressure measurements were estimated to be ±0.2°C and ±1 kPa, respectively. More details regarding the experimental setup can be found in Zeitoun and Shoukri.[19] Experimental conditions used for comparison with the simulated results are presented in Table 4. Figure 4b shows a schematic drawing of the test channel.

Numerical Details

Solutions to the two sets of governing equations for the balance of mass, momentum, and energy of each phase were sought. The conservation equations were discretized using the control volume technique. The discrete bubble sizes, prescribed in the dispersed phase, were further tracked by solving an additional set of 15 transport equations, which were progressively coupled with the flow equations during the simulations. The velocity–pressure linkage was handled through the SIMPLE procedure. The discretized equations were solved using Stone's Strongly Implicit Procedure.[41] Because the wall heat flux was applied uniformly throughout the inner wall of

the annulus, the advantage of the annular geometrical shape was used by modeling only one quarter of the annulus as the domain for simulation for both the local and axial cases. A body-fitted conformal system was used to generate the three-dimensional mesh within the annular channel, resulting in a total of 13 (radial) × 30 (height) × 3 (circumference) control volumes for the local case, whereas a total of 8 (radial) × 20 (height) × 3 (circumference) control volumes resulted for the axial case. Because wall function was used in the present study, the normal distance between the wall and the first node in the bulk liquid should be such that the corresponding y^+ was >30. Grid independence was examined. In the mean parameters considered, further grid refinement did not reveal significant changes to the two-phase flow parameters. Convergence was achieved within 1500 iterations when the mass residual dropped below 1×10^{-7}. Global execution time on a Silicon Graphics machine was about 30 min.

Results and Discussion

### Empirical bubble diameter relationship for local comparison

The radial profiles of the bubble Sauter diameter, void fraction, IAC, and vapor and liquid velocities, located at 1.61 m downstream of the beginning of the heated section, are predicted through the two-fluid and MUSIG boiling models. In all the figures presented for the local case, the dimensionless parameter $(r - R_i)/(R_o - R_i) = 1$ indicates the inner surface of the unheated flow channel wall, whereas $(r - R_i)/(R_o - R_i) = 0$ indicates the surface of the heating rod in the annulus channel.

The MUSIG boiling model predictions against local measurements are also compared with computational results determined through the empirical relationship advanced by Anglart and Nylund[22] to determine the local bubble diameter. They proposed to estimate the interfacial transfer terms through a bubble diameter relationship, assuming a linear dependency with local liquid subcoolings, which can be expressed by

$$d = \frac{d_l(\theta_{sub} - \theta_0) + d_0(\theta_l - \theta_{sub})}{\theta_1 - \theta_0} \quad (31)$$

This relationship is still currently being used and applied in many boiling studies through the CFX code. Application of this correlation for subcooled boiling flow at low pressures has recently been reported in the numerical investigations of Lee et al.[16]

Reference diameters of d_0 and d_1 in Eq. 31, corresponding to the reference subcooling temperatures at θ_0 and θ_1, are usually not known a priori. Calculations based on different reference diameters have been investigated in the present study. We have assumed for the first case—"Linear1"—that the local bubble diameters were evaluated between $d_0 = 1.5 \times 10^{-4}$ m and $d_1 = 4.0 \times 10^{-3}$ m, whereas for the second case—"Linear2"—
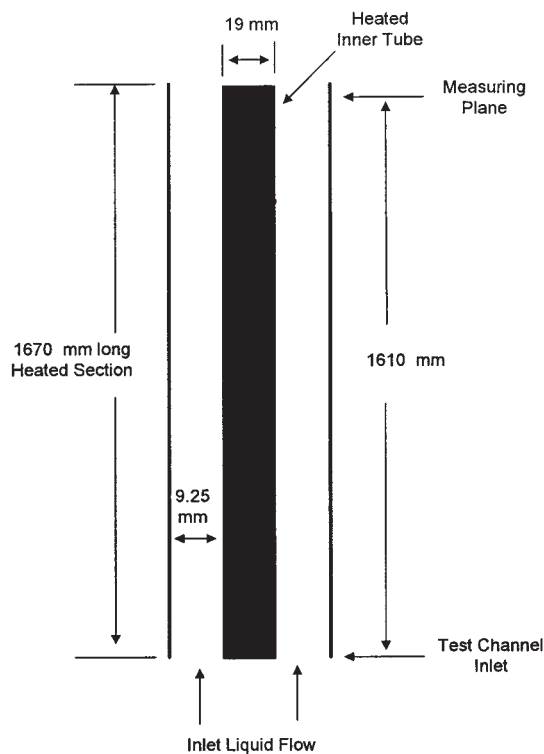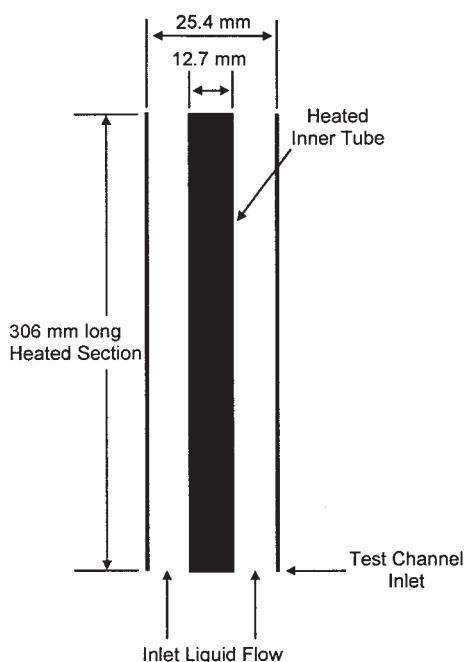
Figure 4. Test channel.

(a) Local measurements and (b) axial measurements.

they are determined between $d_0 = 1.5 \times 10^{-4}$ m and $d_1 = 7.0 \times 10^{-3}$ m, respectively. We further assumed that both of the reference diameters corresponded to identical reference subcooling temperatures of $\theta_0 = 13.0$ K and $\theta_1 = -5$ K.

Local distributions of the bubble Sauter diameter, void fraction, and interfacial area concentration

Figure 5 illustrates the local radial bubble Sauter diameter distribution at the measuring plane of the heated annular channel. In all three cases, the empirical correlations from Anglart and Nylund[22] misrepresented the local bubble size distribution. The gradual increase of the bubble Sauter diameters toward the heated wall with the highest bubble sizes predicted at the heated wall by the empirical relationships contradicted the local radial measurements. In the experiments, high-speed photography (see Figure 2) clearly demonstrated that large bubble sizes were present away from the heated wall, not at the heated wall. This trend was correctly predicted by the MUSIG boiling model. Good agreement was achieved against the measured bubble sizes for all three experimental conditions. The predicted bubble diameter behavior determined through the empirical correlation was determined to be deficient because of the absence of properly accommodating the bubble mechanistic behavior of coalescence and collapse attributed to condensation. Evidently, the bubble size determination in the bulk liquid core was not strictly dependent on only local subcoolings. The empirical relationship was seen to significantly compromise the model predictions.

It was also observed in Lee et al.[16] that the vapor bubbles, relatively small when detached from the heated surface, increased in size because of bubble coalescence as they migrated toward the center of the flow channel. The bubble departure diameter evaluated from Eq. 27 resulted in a bubble size of about 1.8 mm. In all three cases compared, a maximum predicted bubble size for L1, L2, and L3 of about 4.5, 4.0, and 3.8 mm, respectively, confirmed the experimental observations. It was also interesting to note that coalescence of bubbles occurred axially along the heated surface. Experiments by Bonjour and Lallemand[42] and Prodanovic et al.[43] clearly indicated the presence of bubbles sliding shortly after being detached from the heated cervices before lifting into the liquid core. These upstream bubbles traveling closely to the heated wall have the tendency of significantly colliding with any detached bubbles downstream and subsequently forming bigger bubbles as a result of the bubbles merging together. Here, simulations have determined a bubble Sauter diameter of 3 mm, corresponding to the adjacent points along the heated wall for all three experimental conditions L1, L2, and L3. That the bubble sizes are substantially larger than the bubble departure diameter demonstrated to some degree the capability of the MUSIG boiling model to capture the coalescence behavior of the bubbles sliding along the heated surface.

As the bubbles migrated toward the opposite end of the adiabatic wall, they are decreased because of the increased condensation. Here, only the *low-temperature* single-phase subcooled water existed. The bubble Sauter diameter profiles of the MUSIG boiling model clearly showed the gradual collapse of the bubbles and the absence of bubbles near the adiabatic wall of the test channel. Important insights to the effect of condensation revealed that more bubbles were condensed at a higher inlet subcooling condition as shown in Figure 5c. With increasing mass fluxes, the interfacial heat

Table 4. Experimental Conditions for Axial Measurements: A1 and A2

Run	P_{inlet} (MPa)	T_{inlet} (°C)	T_{sub}(inlet) (°C)	Q_w (kW/m^2)	G (kg m^{-2} s^{-1})
A1	0.15	94.6	16.6	508.0	264.34
A2	0.15	88.9	22.5	705.0	411.7

transfer was further enhanced, thereby resulting in more bubbles being condensed in the subcooled liquid core.

Figure 6 presents the locally predicted void fraction profiles against radial measured values. The peak local void fraction was always observed in the vicinity of the heated surface in a typical subcooled boiling flow. This high local void fraction found here was explicitly attributed to the large number of bubbles generated from the active nucleation sites on the heated surface. Here, a substantial amount of bubbles was generated from these nucleation sites when the temperature on the heated surface exceeded the saturation temperature. As these bubbles reached a critical size, they detached and migrated laterally toward the subcooled liquid core under the competing process of bubble coalescence and condensation as mentioned earlier.

The use of "Linear1" reference diameters in Eq. 28 significantly underpredicted the local void fraction distribution for all the experimental conditions. By using a larger reference diameter of d_1 in "Linear2," the predictions faired better. Albeit its simplicity of formulation and application, the use of this relationship failed to offer any significant benefits attributed to the ad hoc specifications of its reference diameters.

In some boiling problems, the setting of proper reference subcooling limits needs to be carefully selected, which are also not known a priori. More important, extending the use of this empirical relationship for other types of boiling flow regimes may not be confidently applied beyond the subcooled bubbly flow regime, flow transition in the two-phase flow structures from bubbly to slug or churn turbulent boiling regimes, and other geometry configurations. However, the MUSIG boiling model (fundamentally derived from population balance principles) has the capacity of accommodating the different ranges of bubble sizes and mechanisms that may be present within the boiling liquid. It thus presents enormous potential of possibly tracking the transition from one flow regime to another and mechanistically predicting the bubble sizes associated with each of the boiling flow regimes. This approach may well replace traditional flow regime maps and regime transition criteria. For example, numerical studies of adiabatic bubbly flows in bubble columns, conducted by Olmos et al.,[5] have demonstrated the capability of the MUSIG model to predict the evolution of bubble sizes between two flow domains. In these two domains, the characteristics of the bubbles are typical of the homogeneous and transition regimes.

Figure 7 describes the local IAC radial distribution. The IAC can be determined through the following relationship

$$a_{if} = \frac{6\alpha_g}{D_s} \qquad (32)$$

The measured radial data followed a trend similar to that of the void fraction distribution in Figure 7. The use of smaller reference diameters in "Linear1" significantly overpredicted the IAC near the heated wall, as expected. Overall, better agreement between the measured and predicted IAC was achieved using the MUSIG boiling model. Based on a recent investigative study, Hibiki and Ishii[44] established the significance of active wall nucleation site density linking to the prediction of the IAC. A generalized expression of the active nucleation site density on the heated surface covering a wide range of conditions is still not available and requires more analysis, especially for large mass fluxes. One complexity that arises in performing such experiments is in determining the population distribution of cavities, which cannot be directly determined by measurement; they have to be indirectly inferred from experimental data. The local predictions of the void fraction and bubble Sauter diameter and consequently IAC immediately adjacent to the heated surface were determined through imposed boundary conditions at the heated surface. Therefore, they were greatly influenced by the density of the active wall nucleation sites and to some degree by the bubble departure size at the wall, which explained the discrepancies seen in Figure 7. Empirical correlation applied as a simpler boiling model was developed, void of any direct influence from the heated surface boundary conditions. Predictions made through this relationship may again not be easily extendable beyond general boiling flow structures.

Local distributions of the vapor and liquid velocities

The radial profiles of the axial component of the local vapor velocity are shown in Figure 8, whereas Figure 9 presents the radial profiles of the local liquid velocity for experimental conditions L1, L2, and L3.

The vapor velocity was greater than the liquid velocity because of buoyancy force caused by density difference. As was observed in the experiment, the vapor velocity was higher at the center than the velocities near the heating rod. This was probably attributable to the buoyancy effect being enhanced for the migration of the large bubbles there, which was again confirmed by high-speed photography in Lee et al.[16] However, the vapor velocity predicted by the MUSIG boiling model along with local empirical bubble diameter relationship for calculating the local bubble sizes showed higher velocity values approaching the heated boundary. The MUSIG boiling model vapor velocities in the vicinity of the heated surface were rather similar to those of the simpler models for all three cases because of the assumption that each bubble class traveled at the same mean algebraic velocity. The philosophy behind adopting this approach for the subcooled boiling studies was to hasten the computational time and reduce computational resources. However, the discrepancies between the predicted and measured velocities near the heated wall demonstrated the inadequacy of the adopted approach. Within the channel space, different size bubbles are expected to travel with different speeds. As an initial step toward resolving the problem, additional momentum equations or an algebraic slip model could be proposed to account for bubble separation. For the latter, the terminal velocities for each of the bubbles can be considered by applying an algebraic relationship suggested by Clift et al.,[45] which are then used to evaluate the individual bubble slip velocities. Work is
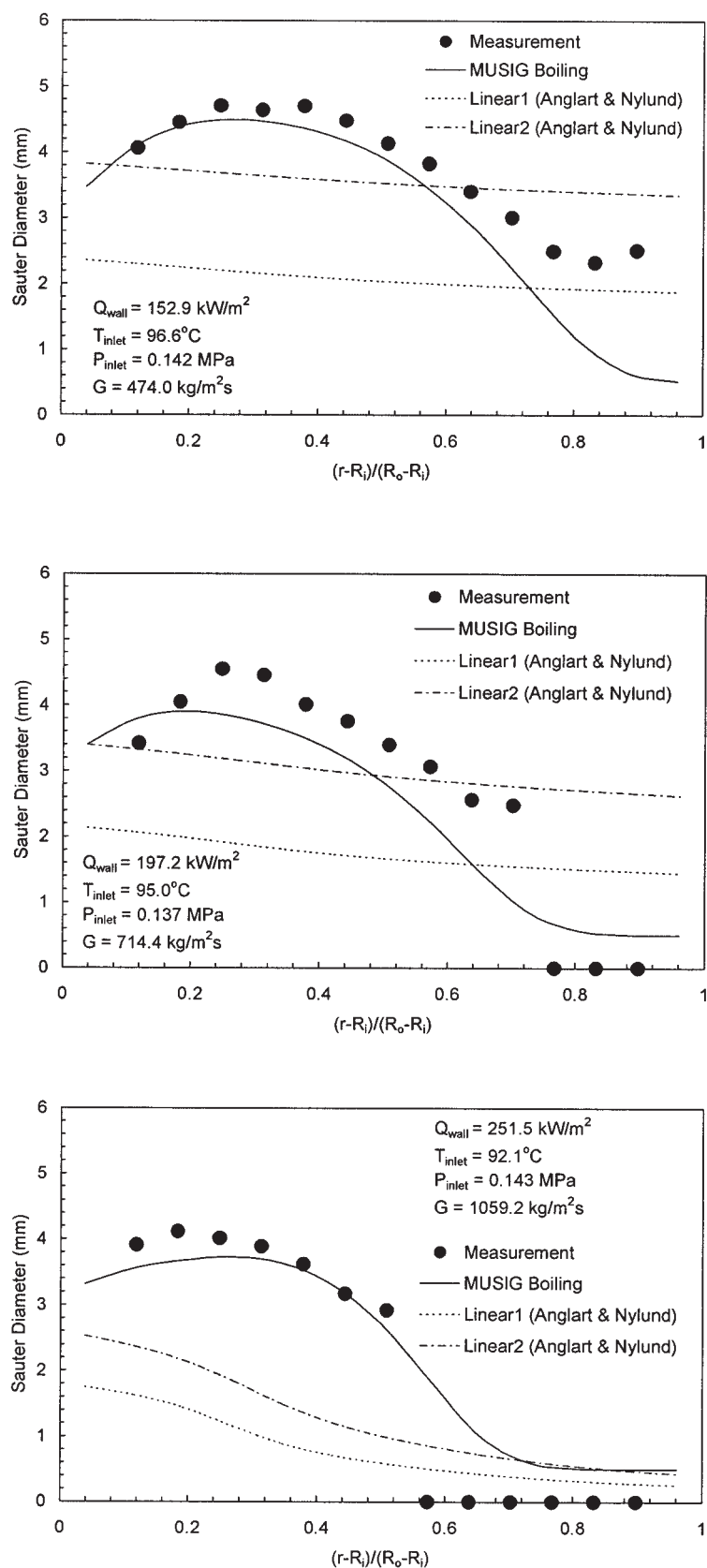
Figure 5. Local mean radial profiles of bubble Sauter diameter.
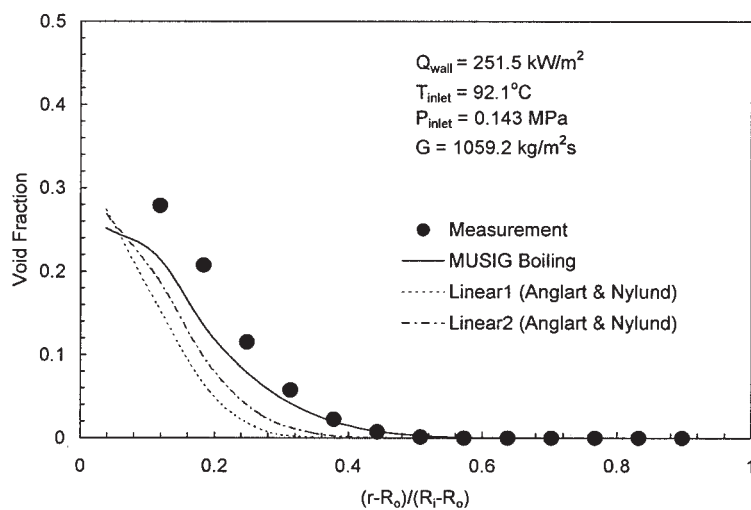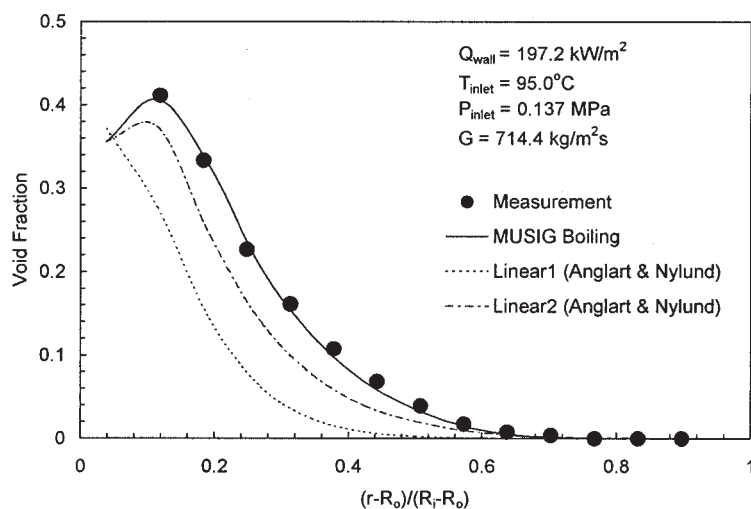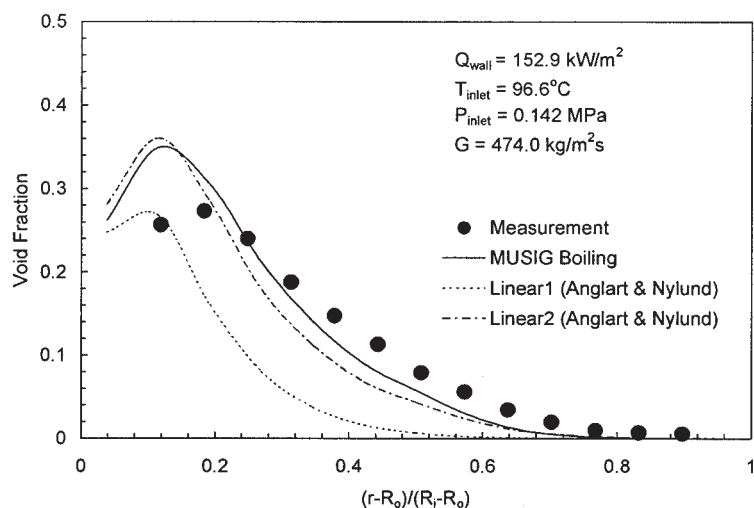(a) L1, (b) L2, and (c) L3.

Figure 6. Local mean radial profiles of void fraction.
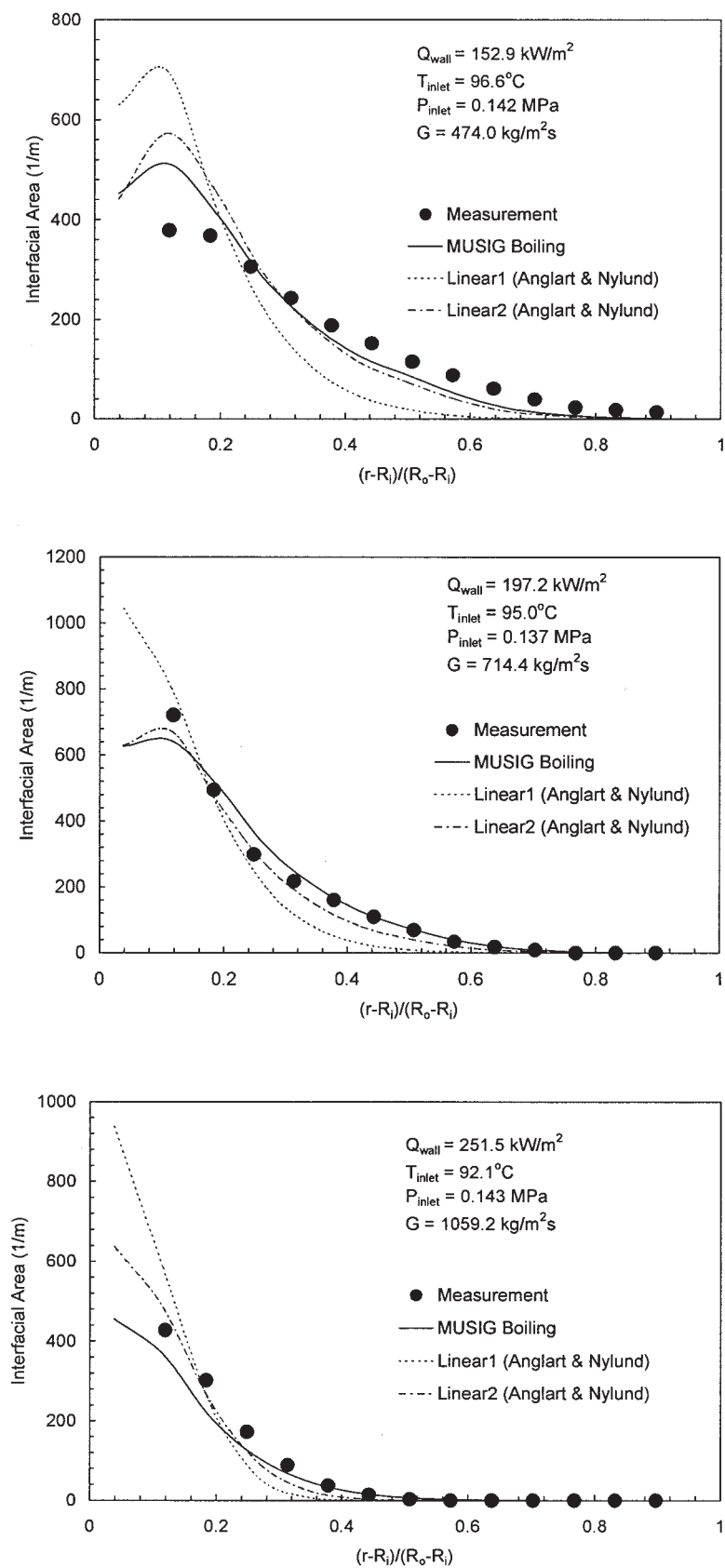(a) L1, (b) L2, and (c) L3.

Figure 7. Local mean radial profiles of interfacial area concentration.
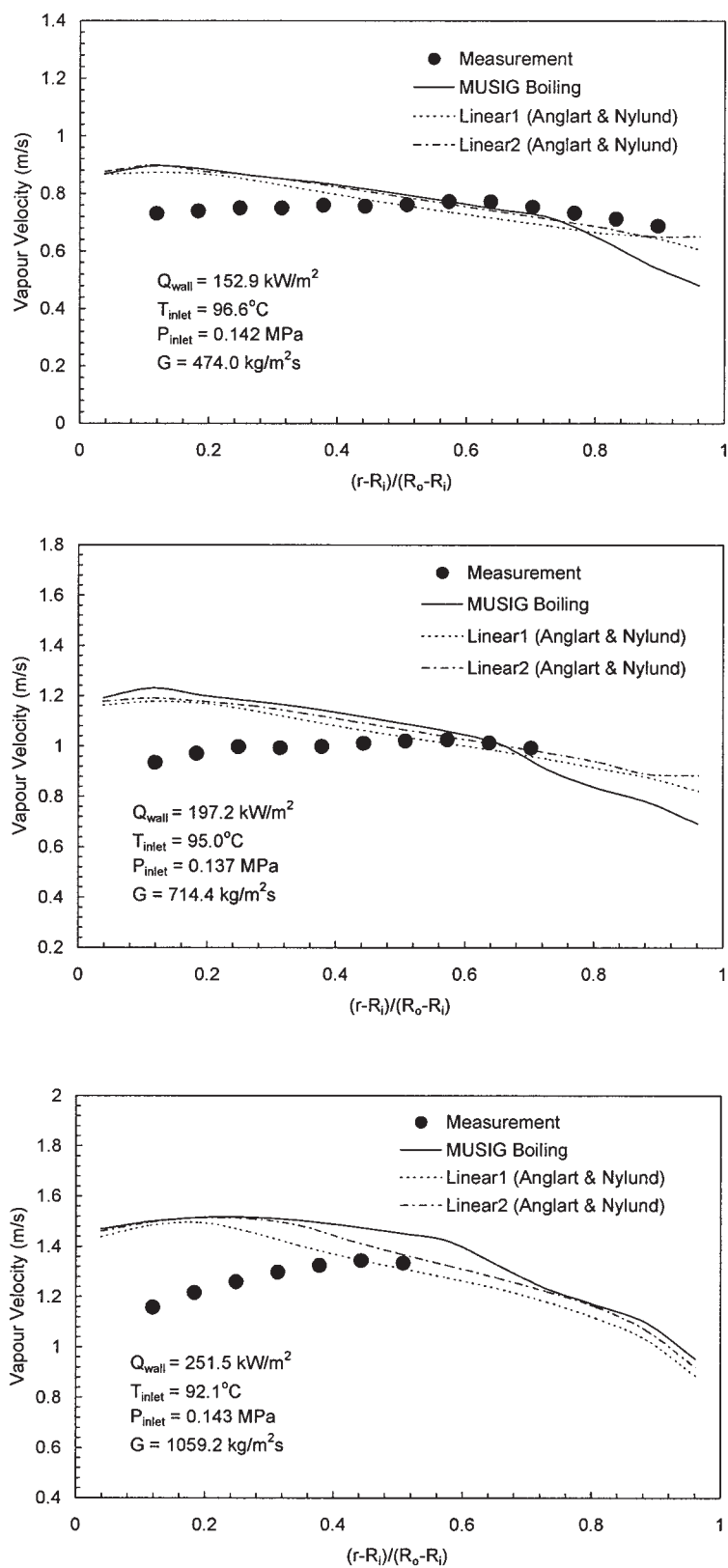(a) L1, (b) L2, and (c) L3.

Figure 8. Local mean radial profiles of vapor velocity.
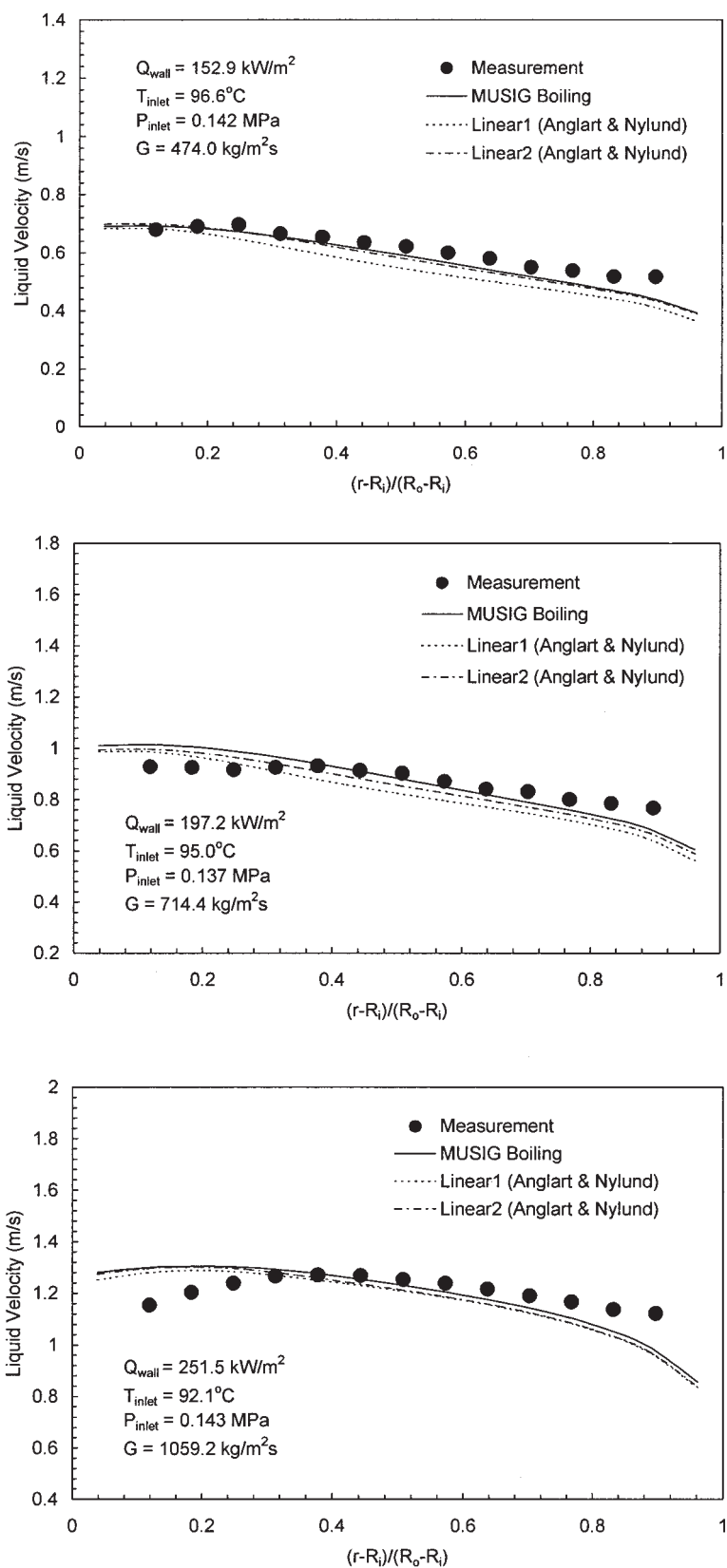(a) L1, (b) L2, and (c) L3.

Figure 9. Local mean radial profiles of liquid velocity.
(a) L1, (b) L2, and (c) L3.

currently in progress to overcome this deficiency of the two-fluid and MUSIG boiling models. The consideration of additional momentum equations to cater to each of the 15 bubble classes would increase the computational resources tremendously and is deemed impractical. Ongoing investigations are currently being undertaken to test a pertinent choice of two or three dominant groups of bubbles transformed into the Eulerian phases to sufficiently accommodate the hydrodynamics of bubbly flows of widely distributed bubble sizes. Also, the process of developing an algebraic slip model is in progress to account for the proper evaluation of slip velocities resulting from bubble separation.

Nevertheless, in Figure 9, good agreement achieved for the liquid velocities, between the predictions and experimental values, at the measuring plane in the liquid phase was gratifying. These velocities showed a closer resemblance to the measurements than the predicted profiles of the vapor velocity.

Axial distributions of the mean and local bubble Sauter diameter, interfacial area concentration, and void fraction

For the axial case, the experimental data of Zeitoun and Shoukri[19] (here, cases A1 and A2) have been used to examine the effect of various parameters and models on the numerical predictions. These data were chosen because they provided measurements of the mean bubble Sauter diameter distribution along the axial length, which allowed direct verification of the MUSIG boiling model in predicting the axial evolution of the bubble size.

Figure 10 compares the measured and predicted bubble diameters normalized by the length scale $\sqrt{\sigma/g\Delta\rho}$ along the heated section. Good agreement was achieved comparing the axially computed area-averaged bubble Sauter diameter determined through the MUSIG boiling model against the measured values. The increasing bubble sizes along the axial length clearly showed the intensification of the bubble coalescence as the bubbles traveled downstream along the heated wall toward the channel exit. Because of the high heat fluxes imposed, the ONB point occurred at the channel entrance. Between the ONB point and a channel height of 0.1 m downstream, the larger bubble diameters predicted for both cases in this region were attributed to the constant bubble departure diameter prescribed for the wall heat partition model, which subsequently yielded higher evaporation mass transfer rates at the heated surface. Beyond the channel height of 0.1 m, the dominance of bubble coalescence preceded the influence of the bubble departure at the wall. The coalescence intensity reached the highest around the channel exit. Figure 11 illustrates the local radial distribution of the bubble Sauter diameters at three respective locations along the channel height: near the channel entrance, middle of the channel, and near the channel exit. At these three locations for both cases, the bubbles showed an increased tendency for vigorous coalescence as they migrated downstream, particularly close to the channel exit. The presence of large bubbles blanketing the channel space near the channel exit, especially for case A1, indicated the possible existence of different flow regimes. Flow visualizations using high-speed video revealed a flow regime transition from bubbly flow to churn flow, for which the numerical simulations are in agreement with the observed phenomena. In Figure 11, it could also be inferred that bubble interaction or coalescence was not the major mech-

anism in the vicinity of the channel entrance, at which the local radial bubble distribution indicated the bubbles condensing more favorably because of the higher subcooling temperatures.

Figure 12 describes the axial IAC distribution, whereas Figure 13 demonstrates the axial void fraction evolution along the heated section. Because of the good agreement achieved between the predictions and measurements of the void fraction, the IAC were also in good agreement with the measured values, for the given axial bubble size evolution. The predicted void fraction profiles clearly represented the subcooled boiling characteristics as depicted in Figure 1: a low void fraction region followed by a second region, in which the void fraction increased significantly. The predicted void fraction profiles also correctly established a plateau at the initial stages of boiling. The sharp increase of the void fraction profiles approaching the channel exit was attributed to the increase of bubble sizes decreasing the IAC, thereby causing a reduction in the condensation rate per unit volume of the channel. Also, this was also associated with the reduction in the relative importance of condensation at the bubble interface resulting from the decrease of liquid subcooling, which encouraged more bubbles to merge. The point separating between the low and high void fraction regions were described earlier as the NVG point. During experiments, they were measured to be at axial distances of 7.5 and 9.2 cm from the channel entrance with an uncertainty of ± 2 cm, respectively. This large uncertainty clearly highlighted the difficulty in precisely locating the point where bubbles became significantly detached from the heating surface. Rogers et al.[46] performed special experiments to determine the void content at the onset of significant voiding and established that the void content at the NVG lay between 5 and 10%. Based on a void content of 7.5%, an average value between 5 and 10%, the axial distances of the NVG point for cases A1 and A2 were determined to be 6.6 and 5.7 cm, respectively. It is noted that accurate determination of the NVG points is a subject of constant debate. However, the close agreement between the predicted and measured NVG points was gratifying.

Conclusion

A two-fluid model, coupled with a population balance approach, is presented in this article to handle bubbly flows in the presence of heat and mass transfer processes. The increase in complexity of modeling such flows derives from the additional consideration of the gas or liquid undergoing a phase transformation. Subcooled boiling flow belongs to a specific category of bubbly flows with heat and mass transfer, where it embraces all the complex dynamic interaction of the phenomena associated with hydrodynamics, heat and mass transfer, and coalescence and breakup of bubbles. Modeling subcooled boiling flows, particularly at low pressures, have been successfully demonstrated. The range of bubble sizes in the subcooled boiling flow was distributed according to the division of 15 diameter classes. Each of them experiencing coalescence and breakup phenomena has been considered. The MUSIG boiling model was developed to account for the wall nucleation or vapor generation on the heated surface and condensation process in the subcooled liquid core combined with the bubble coalescence of Prince and Blanch[30] and bubble breakup of Luo and Svendsen.[31]

Comparison of the predicted results was made against local measurements of Yun et al.[20] and Lee et al.[16] An additional comparison, using an empirical relationship to determine the
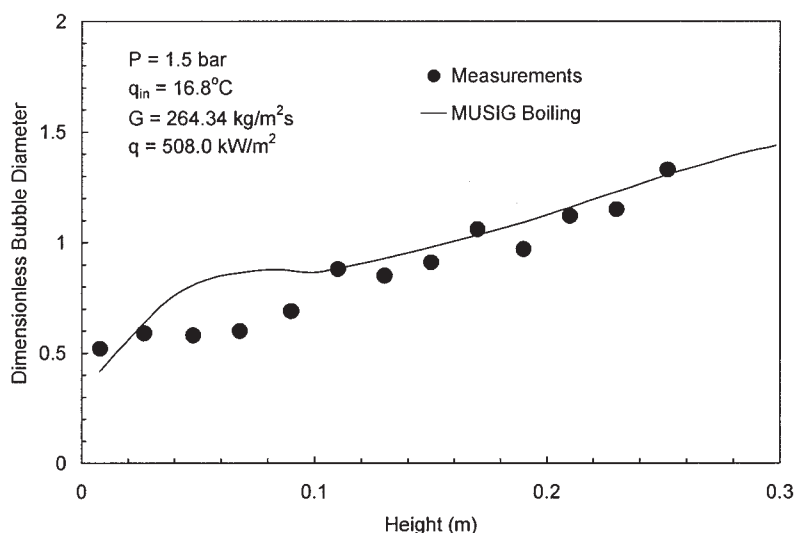
(a)
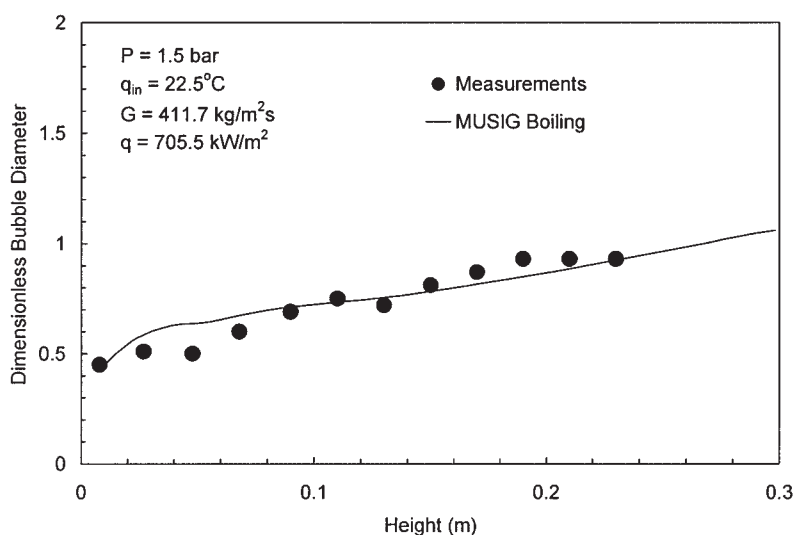
(b)

**Figure 10. Axial distribution of the mean bubble diameter.**

(a) A1 and (b) A2.

local bubble diameter adopted in the CFX boiling model, was also investigated. Good agreement was achieved through the newly formulated MUSIG boiling model for the local bubble Sauter diameter, void fraction, IAC, and liquid velocity profiles. However, in the gas phase, given that the assumption was invoked where each bubble class traveled at the same mean algebraic velocity to reduce the computational time and resources, a weakness of the model was evidenced in the prediction of the vapor velocity. Research is currently ongoing to consider additional momentum equations or develop an algebraic slip model to account for bubble separation, to yield a more realistic prediction of the vapor velocity.

Comparison of the predicted results was also made against axial measurements of Zeitoun and Shoukri.[19] Good agreement was achieved for the mean bubble Sauter diameter, IAC, and void fraction profiles. The MUSIG boiling model clearly represented the plateau at the initial boiling stages, typical of subcooled flow boiling at low pressures, followed by the significant increase of the void fraction downstream. Work is in progress to address the discrepancy evidenced in the formation of bubbles in the bulk subcooled liquid during the initial stages of boiling through the formulation of a model to better predict the bubble departure along the heated section through consideration of appropriate forces acting on them.
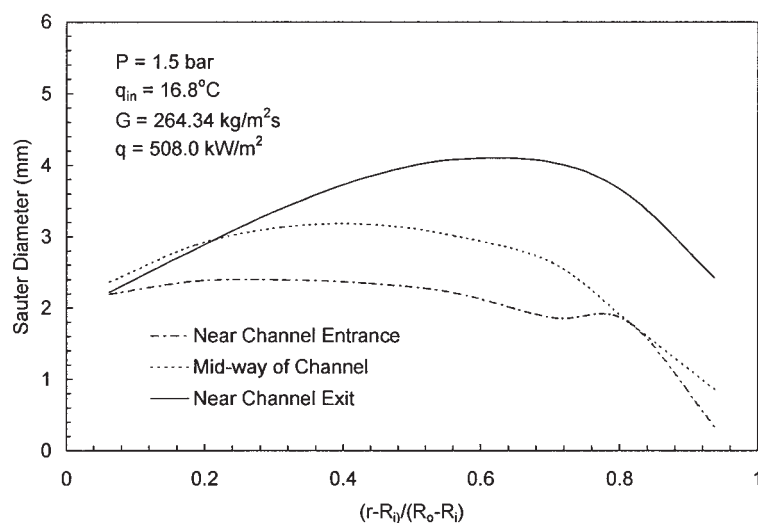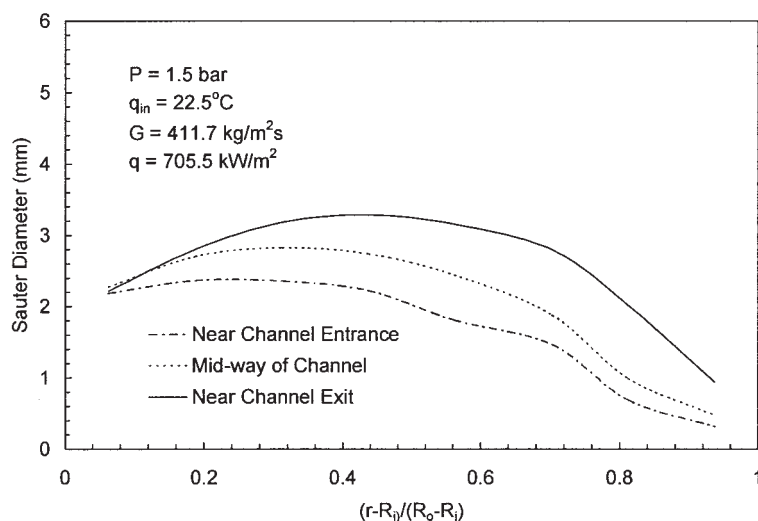
Figure 11. Local radial profiles of bubble Sauter diameter.

(a) A1 and (b) A2 at three locations: near the channel entrance, midway of channel and, near the channel exit.

Notation

a_{if} = interfacial area concentration
A_B = bubble area
A_C = cross-sectional area of boiling channel
A_q = fraction of wall area subjected to quenching
c_f = increase coefficient of surface area
C = constant in Eq. 17
C_p = specific heat
C_D = drag coefficient
C_L = lift coefficient
C_{TD} = turbulent dispersion coefficient
$C_w1, Cw2$ = wall lubrication constants
d = parent particle diameter
d_{bw} = bubble departure diameter
$d_{i, dj}$ = daughter particle diameters

d_{ij} = equivalent diameter
$d_0, d1$ = reference bubble diameters
D_B = death rate due to breakup
D_C = death rate due to coalescence
D_s = bubble Sauter diameter
f = bubble departure frequency
f_{BV} = breakage volume fraction
f_i = scalar variable of the dispersed phase
F_{lg} = total interfacial force
F_{lg}^{drag} = drag force
F_{lg}^{lift} = lift force
$F_{lg}^{lubrication}$ = wall lubrication force
$F_{lg}^{dispersion}$ = turbulent dispersion force
g = gravitational acceleration
$\tilde{g}$ = gravitational vector
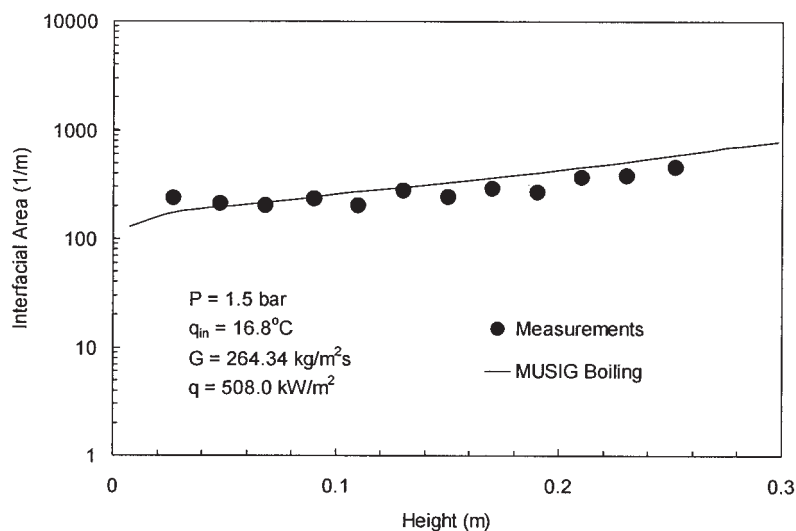
(a)
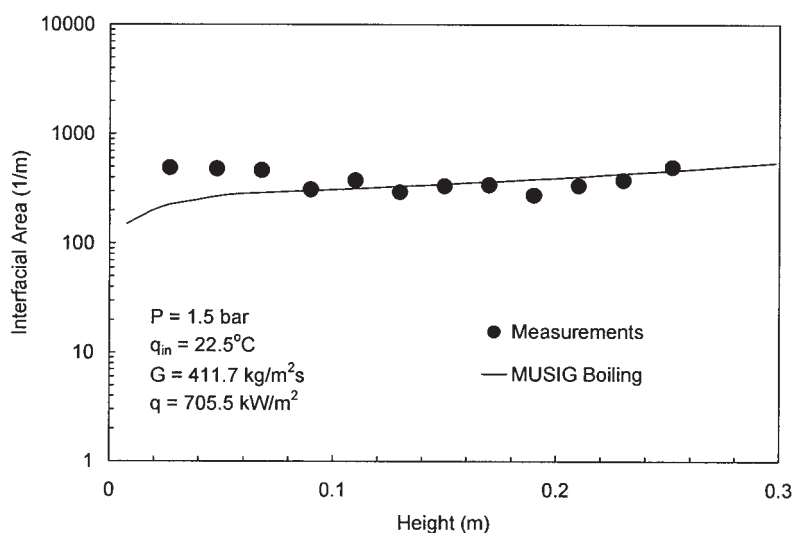
(b)

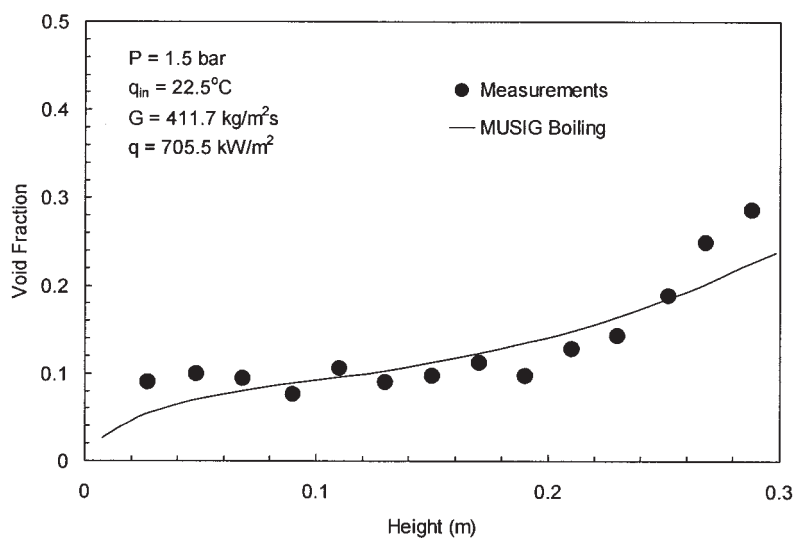**Figure 12. Axial distribution of the interfacial area concentration.**

(a) A1 and (b) A2.

h = interphase heat transfer coefficient		Q = heat source in Eq. 4	
G = mass flux		Q_w = wall heat flux	
$G(V, x, t)$ = generation function		Q_c = heat transferred by convection	
h = initial film thickness		Q_e = heat transferred by evaporation	
h_f = critical film thickness at rupture		Q_q = heat transferred by quenching	
h_{fg} = latent heat		r = radius	
H = enthalpy		R_B = bubble radius	
k = turbulent kinetic energy		$R_{i,o}$ = inner and outer radius of annular channel	
$\vec{n}$ = normal to the wall surface		R_{ph} = source/sink term due to phase change	
$n(V, x, t)$ = bubble number density distribution		S_i = source/sink term due to coalescence and breakup	
n_i = number density of the ith class		St = Stanton number	
n_j = number density of the jth class		t = thermo-fluid timescale	
N = number of bubble classes		t_{ij} = coalescence time	
N'' = active nucleation site density		T = temperature	
P = pressure		T_{sat} = saturation temperature	
P_B = production rate due to breakup		T_{sub} = subcooling temperature	
P_C = production rate due to coalescence		u = velocity	
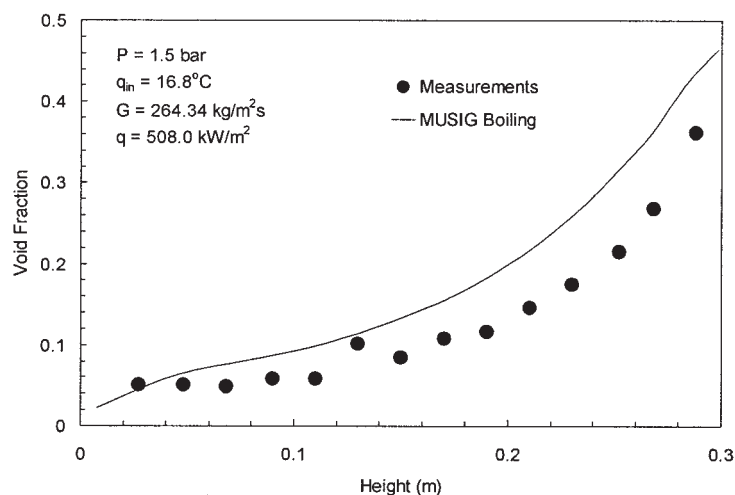
(a)

(b)

Figure 13. Axial distribution of the void fraction.

(a) A1 and (b) A2.

$\vec{u}$ = velocity vector
u_t = velocity due to turbulent collision
v = volume corresponding to particle diameter d
V_B = bubble volume
$\tilde{x}$ = spatial vector
y_w = adjacent point normal to the wall surface

Greek letters

α = void fraction
β = measured constant in Eq. 17
χ = coalescence rate
ε = dissipation of kinetic energy
ϕ_{WN} = bubble nucleation rate
ϕ_{COND} = bubble condensation rate
κ = turbulent kinetic energy

Γ = mass transfer
λ = size of an eddy
λ^e = effective thermal conductivity
μ^e = effective viscosity
θ = bubble contact angle
θ_{ij} = turbulent collision rate
θ_{sub} = subcooling temperature = $T_{sat} - T_l$
θ_0, θ_1 = reference subcooling temperatures in Eq. 28
ρ = density
$\Delta\rho$ = density difference = $\rho_l - \rho_g$
σ = surface tension
τ_{ij} = bubble contact time
Ω = breakup rate
ξ = size ratio between an eddy and a particle in the inertial subrange
ξ_H = heated perimeter of boiling channel

Subscripts

g = vapor
gl = transfer of quantities from liquid phase to vapor phase
l = liquid
lg = transfer of quantities from vapor phase to liquid phase
min = minimum
w = wall

Literature Cited

1. Ramkrishna D, Mahoney AW. Population balance modeling. Promise for the future. *Chemical Engineering Science.* 2002;57:595-606.
2. Krishna R, Urseanu MI, van Baten JM, Ellenberger J. Influence of scale on the hydrodynamics of bubble columns operating in the churn-turbulent regime: Experiments vs. Eulerian simulations. *Chemical Engineering Science.* 1999;54:4903-4911.
3. Shimizu K, Takada S, Minekawa K, Kawase Y. Phenomenological model for bubble column reactors: Prediction of gas hold-up and volumetric mass transfer coefficients. *Chemical Engineering Journal.* 2000;78:21-28.
4. Pohorecki R, Moniuk W, Bielski P, Zdrojkwoski A. Modelling of the coalescence/redispersion processes in bubble columns. *Chemical Engineering Science.* 2001;56:6157-6164.
5. Olmos E, Gentric C, Vial Ch, Wild G, Midoux N. Numerical simulation of multiphase flow in bubble column reactors. Influence of bubble coalescence and break-up. *Chemical Engineering Science.* 2001;56:6359-6365.
6. Wu Q, Kim S, Ishii M, Beus SG. One-group interfacial area transport in vertical bubbly flow. *International Journal of Heat and Mass Transfer.* 1998;41:1103-1112.
7. Hibiki T, Ishii M. Two-group area transport equations at bubbly-to-slug flow transition. *Nuclear Engineering and Design.* 2000;202:39-76.
8. Hibiki T, Ishii M. Development of one-group interfacial area transport equation in bubbly flow systems. *International Journal of Heat and Mass Transfer.* 2002;45:2351-2372.
9. Hibiki T, Ishii M, Xiao Z. Axial interfacial area transport of vertical bubbly flows. *International Journal of Heat and Mass Transfer.* 2001; 44:1869-1888.
10. Ishii M, Kim S, Uhle J. Interfacial area transport equation: Model development and benchmark experiments. *International Journal of Heat and Mass Transfer.* 2002;45:3111-3123.
11. Milles M, Mewes D. Interfacial area density in bubbly flow. *Chemical Engineering and Processing.* 1999;38:307-319.
12. Lehr F, Mewes D. A transport equation for the interfacial area density applied to bubble columns. *Chemical Engineering Science.* 2001;56: 1159-1166.
13. Tu JY, Yeoh GH. On numerical modelling of low-pressure subcooled boiling flows. *International Journal of Heat and Mass Transfer.* 2002; 45:1197-1209.
14. Yeoh GH, Tu JY. Implementation of a two-phase boiling model into the RELAP/MOD2 computer code to predict void distribution in low-pressure subcooled boiling flows. *Nuclear Science and Engineering.* 2002;140:182-188.
15. Yeoh GH, Tu JY, Lee TH, Park G-C. Prediction and measurement of local two-phase flow parameters in a boiling flow channel. *Numerical Heat Transfer Part A: Applications.* 2002;42:173-192.
16. Lee TH, Park G-C, Lee DJ. Local flow characteristics of subcooled boiling flow of water in a vertical annulus. *International Journal of Multiphase Flow.* 2002;28:1351-1368.
17. Gopinath R, Basu N, Dhir VK. Interfacial heat transfer during subcooled flow boiling. *International Journal of Heat and Mass Transfer.* 2002;45:3947-3959.
18. Lo S. Application of population balance to CFD modelling of bubbly flow via the MUSIG model. *AEA Technology.* 1996;AEAT-1096.
19. Zeitoun O, Shoukri M. Bubble behavior and mean diameter in subcooled flow boiling. *ASME Journal of Heat Transfer.* 1996;118:110-116.
20. Yun BJ, Park G-C, Song CH, Chung MK. Measurements of local two-phase flow parameters in a boiling flow channel. Proceedings of the OECD/CSNI Specialist Meeting on Advanced Instrumentation and Measurement Techniques, Mar. 17–20, Santa Barbara, CA; 1997.
21. Ranz WE, Marshall WR. Evaporation from droplets: Parts I and II. *Chemical Engineering Progress.* 1952;48:141-148.
22. Anglart H, Nylund O. CFD application to prediction of void distribution in two-phase bubbly flows in rod bundles. *Nuclear Science and Engineering.* 1996;163:81-98.
23. Lahey RT Jr, Drew DA. The analysis of two-phase flow and heat transfer using multidimensional, four field, two-fluid model. *Nuclear Engineering and Design.* 2001;204:29-44.
24. Ishii M, Zuber N. Drag coefficient and relative velocity in bubbly, droplet or particulate flows. *AIChE Journal.* 1979;25:843-855.
25. Wang SK, Lee SJ, Lahey RT Jr, Jones OC. 3-D turbulence structure and phase distribution measurements in bubbly two-phase flows. *International Journal of Multiphase Flow.* 1987;13:327-343.
26. Antal SP, Lahey RT Jr, Flaherty JE. Analysis of phase distribution and turbulence in dispersed particle/liquid flows. *Chemical Engineering Communication.* 1991;174:85-113.
27. Kurul N, Podowski MZ. Multi-dimensional effects in sub-cooled boiling. Proceedings of the Ninth Heat Transfer Conference, Aug. 19–24, Jerusalem, Israel; 1990.
28. Sato Y, Sadatomi M, Sekoguchi K. Momentum and heat transfer in two-phase bubbly flow—I. *International Journal of Multiphase Flow.* 1981;7:167-178.
29. Fleischer C, Becker S, Eigenberger G. Detailed modeling of the chemisorption of CO_2 into NaOH in a bubble column. *Chemical Engineering Science.* 1996;51:1715-1724.
30. Prince MJ, Blanch HW. Bubble coalescence and break-up in air-sparged bubble column. *AIChE Journal.* 1990;36:1485-1499.
31. Luo H, Svendsen H. Theoretical model for drop and bubble break-up in turbulent dispersions. *AIChE Journal.* 1996;42:1225-1233.
32. Chesters AK, Hoffman G. Bubble coalescence in pure liquids. *Applied Scientific Research.* 1982;38:353-361.
33. Rotta JC. Turbulente Stromungen. Stuttgart, Germany: B.G. Teubner; 1972.
34. Judd RL, Hwang KS. A comprehensive model for nucleate pool boiling heat transfer including microlayer evaporation. *ASME Journal of Heat Transfer.* 1976;98:623-629.
35. Cole R. A photographic study of pool boiling in the region of the critical heat flux. *AIChE Journal.* 1960;6:533-542.
36. Kocamustafaogullari G, Ishii M. Foundation of the interfacial area transport equation and its closure relations. *International Journal of Heat and Mass Transfer.* 1995;38:481-493.
37. Lemmert M, Chwala JM. Influence of flow velocity on surface boiling heat transfer coefficient. New York/Washington, DC: Academic Press/Hemisphere; 1977.
38. Basu N, Warrier GR, Dhir VK. Onset of nucleate boiling and active nucleation site density during subcooled flow boiling. *ASME Journal of Heat Transfer.* 2002;124:717-728.
39. Hsu YY, Graham RW. Transport process in boiling and two-phase systems. Washington, DC: Hemisphere; 1976.
40. Bowring RW. Physical model based on bubble detachment and calculation of steam voidage in the subcooled region of a heated channel. *Report HPR-10.* Halden, Norway: Institute for Atomenergi; 1962.
41. Stone HL. Iterative solution of implicit approximations of multidimensional partial differential equations. *SIAM Journal of Numerical Analysis.* 1968;5:530-558.
42. Bonjour J, Lallemand M. Two-phase flow structure near a heated vertical wall during nucleate pool boiling. *International Journal of Multiphase Flow.* 2001;27:1789-1802.
43. Prodanovic V, Fraser D, Salcudean M. Bubble behaviour in subcooled flow boiling of water at low pressures and low flow rates. *International Journal of Multiphase Flow.* 2002;28:1-19.
44. Hibiki T, Ishii M. Active nucleation site density in boiling systems. *International Journal of Heat and Mass Transfer.* 2003;46:2587-2601.
45. Clift R, Grace JR, Weber ME. Bubbles, drops and particles. New York, NY: Academic Press; 1978.
46. Rogers JT, Salcudean M, Abdullah Z, McLeod D. The onset of significant void in up-flow boiling of water at low pressure and velocities. *International Journal of Heat and Mass Transfer.* 1987;30:2247-2260.